# Optical Loss Characterization and Analysis of Wafer-Scale Scandium-Doped AlN Photonic Devices

Yangyang Zhuge[a,b], Wing Wai Chung[a], Yanmei Cao[a], Minghua Li[a], Yat Fung Tsang[a], Yeow Teck Toh[a], Steven Hou Jang Lee[a], Huamao Lin[a], Landobasa Y M Tobing[a,c], Chong Pei Ho[a], Xianshu Luo[a,c], and Chengkuo Lee[b]*, Nanxi Li[a]*

[a]Institute of Microelectronics (IME), Agency for Science, Technology and Research (A*STAR), 2 Fusionopolis Way, Innovis #08-02, Singapore 138634, Republic of Singapore
[b]Center for Intelligent Sensors and MEMS, Department of Electrical and Computer Engineering, National University of Singapore, 4 Engineering Drive 3, Singapore, 117583
[c]National Semiconductor Translation and Innovation Centre (NSTIC), 1 Fusionopolis Way, #19-10 Connexis North, Singapore, 138632

** Corresponding Author: elelc@nus.edu.sg; linx1@a-star.edu.sg*

## ABSTRACT

Scandium-doped aluminum nitride (ScAlN) is a promising material for CMOS-compatible photonic platforms due to its improved material properties and compatibility with wafer-scale processes. In this work, we report the optical loss characteristics of 10% ScAlN thin films deposited via co-sputtering on 8-inch wafers. In addition to device-level characterization, the material properties of the ScAlN films are systematically examined, including top surface roughness measured by atomic force microscopy and optical constants extracted from spectroscopic ellipsometry. Propagation losses are extracted from microring resonators with varying waveguide dimensions, showing a clear trend of increasing loss with larger waveguide width and thickness. This behavior is primarily attributed to increased optical absorption due to mode confinement and variations in material quality. Wafer-level measurements further reveal that waveguides located near the wafer edge exhibit lower losses than those at the center, suggesting improved crystallinity and reduced defect density at the periphery. These results highlight the potential of ScAlN for low-loss, scalable photonic integration.

**Keywords:** Integrated optics devices; Integrated optics materials; Wafer-level characterization; Scandium-doped aluminum nitride.

## INTRODUCTION

Aluminum nitride (AlN) has emerged as an attractive material platform for integrated photonics due to its excellent compatibility with complementary metal–oxide–semiconductor (CMOS) fabrication processes, wide optical transparency window, and intrinsic nonlinear optical properties[1–4]. In particular, AlN supports both second-order ($\chi^2$) and third-order ($\chi^3$) nonlinear effects while offering high optical power handling capability and low two-photon absorption at telecommunication wavelengths [5–9]. These attributes have enabled a broad range of photonic integrated circuit (PIC) functionalities, including frequency conversion, frequency comb generation, acousto-optic modulation, and microwave-to-optical signal processing[10–13]. Moreover, AlN can be deposited at wafer scale using sputtering techniques, making it well suited for large-scale photonic integration[6,14,15]

Despite these advantages, the electro-optic (EO) modulation efficiency of AlN remains fundamentally limited by its relatively weaker Pockels effect compared with other materials with EO effect, e.g. thin film lithium niobate[16–20]. The small intrinsic electro-optic coefficients restrict the achievable modulation efficiency and increase the voltage–length product ($V\pi \cdot L$), posing challenges for compact, low-power modulators[21]. To address this limitation, recent studies have proposed ScAlN as a promising alternative. By incorporating scandium into the AlN lattice, the piezoelectric response can be significantly enhanced, which also leads to an improvement in the effective EO coefficient[22–24]. As a result, ScAlN has attracted increasing interest as a scalable EO material platform for high-efficiency modulation and integrated photonic–electronic systems[24–27].

However, the incorporation of Sc also introduces substantial material and fabrication challenges. As the Sc concentration increases, the crystalline quality of ScAlN thin films tends to degrade, often accompanied by increased defect density, surface roughness, and compositional inhomogeneity. In addition, Sc doping complicates etching processes, making it more difficult to achieve smooth and vertical waveguide sidewalls. These effects collectively lead to increased optical propagation loss, which currently represents one of the major obstacles for practical ScAlN-based photonic integration[28–30]. Consequently, understanding and mitigating optical loss mechanisms in ScAlN waveguides is critical for realizing high-performance EO devices at scale.

To date, most reported studies have focused on chip-level loss characterization, typically extracting propagation losses from waveguides of different widths to infer dominant loss contributions, such as sidewall scattering or material absorption[31–35]. While these approaches provide valuable insights, they offer limited information on thickness-dependent effects and wafer-level uniformity, both of which are crucial for scalable manufacturing.

In this work, we present a comprehensive optical loss characterization of 10% ScAlN thin films using a CMOS-compatible co-sputtering process on 8-inch wafers. In addition to device-level measurements, the material properties of the ScAlN films are characterized by atomic force microscopy (AFM) and spectroscopic ellipsometry, revealing a smooth top surface with sub-nanometer roughness (0.8 nm) and non-negligible optical absorption. Optical propagation losses are extracted from microring resonators fabricated with waveguides of varying widths and thicknesses. For 450 nm thick waveguides, average losses of 11.5, 12.4, 13.2, and 16.4 dB/cm are measured for widths of 0.8, 1.0, 1.5, and 2.0 μm, respectively. Increasing the waveguide thickness to 630 nm introduces an additional loss of approximately 4 dB/cm, suggesting that absorption becomes the dominant loss mechanism. Furthermore, wafer-level measurements reveal systematically lower losses near the wafer edge compared to the center, suggesting spatial variations in film quality and etching process during deposition.

These results provide insights into the interplay between waveguide geometry, material quality, and optical loss in ScAlN photonic devices, and establish design guidelines for wafer-scale, low-loss ScAlN integrated photonic circuits targeting communications, sensing, and computing technologies.

## MATERIAL CHARACTERIZATION OF SCALN THIN FILMS

To assess the material quality of the ScAlN thin films, AFM measurements were performed to characterize the top surface morphology and roughness. Figures 1(a) and 1(b) show the two-dimensional (2D) height map and three-dimensional (3D) surface profile of a representative ScAlN film measured over a 1 × 1 μm² area. The AFM images reveal a dense granular morphology, indicating the polycrystalline nature of the sputtered ScAlN film. From the AFM analysis, the root-mean-square (RMS) surface roughness is measured to be approximately 0.8 nm, suggesting a relatively smooth top surface suitable for PIC applications.

In addition to surface morphology, the optical properties of the ScAlN thin film were characterized by spectroscopic ellipsometry. The extracted refractive index n and extinction coefficient k as a function of wavelength are shown in Figs. 1(c) and 1(d), respectively. Compared with previously reported measurements, the present study covers a broader wavelength range [32]. The refractive index n remains relatively high and shows an increasing trend with higher Sc doping concentration over the measured wavelength range, enabling strong optical confinement for guided modes. Meanwhile, the corresponding extinction coefficient k exhibits non-negligible values, indicating the presence of intrinsic optical absorption in the ScAlN material. Similar to previously reported Sc-doped AlN thin films, an increasing trend of k is observed with higher Sc doping concentration, reflecting enhanced absorption associated with Sc-induced disorder and defect states[22,31].

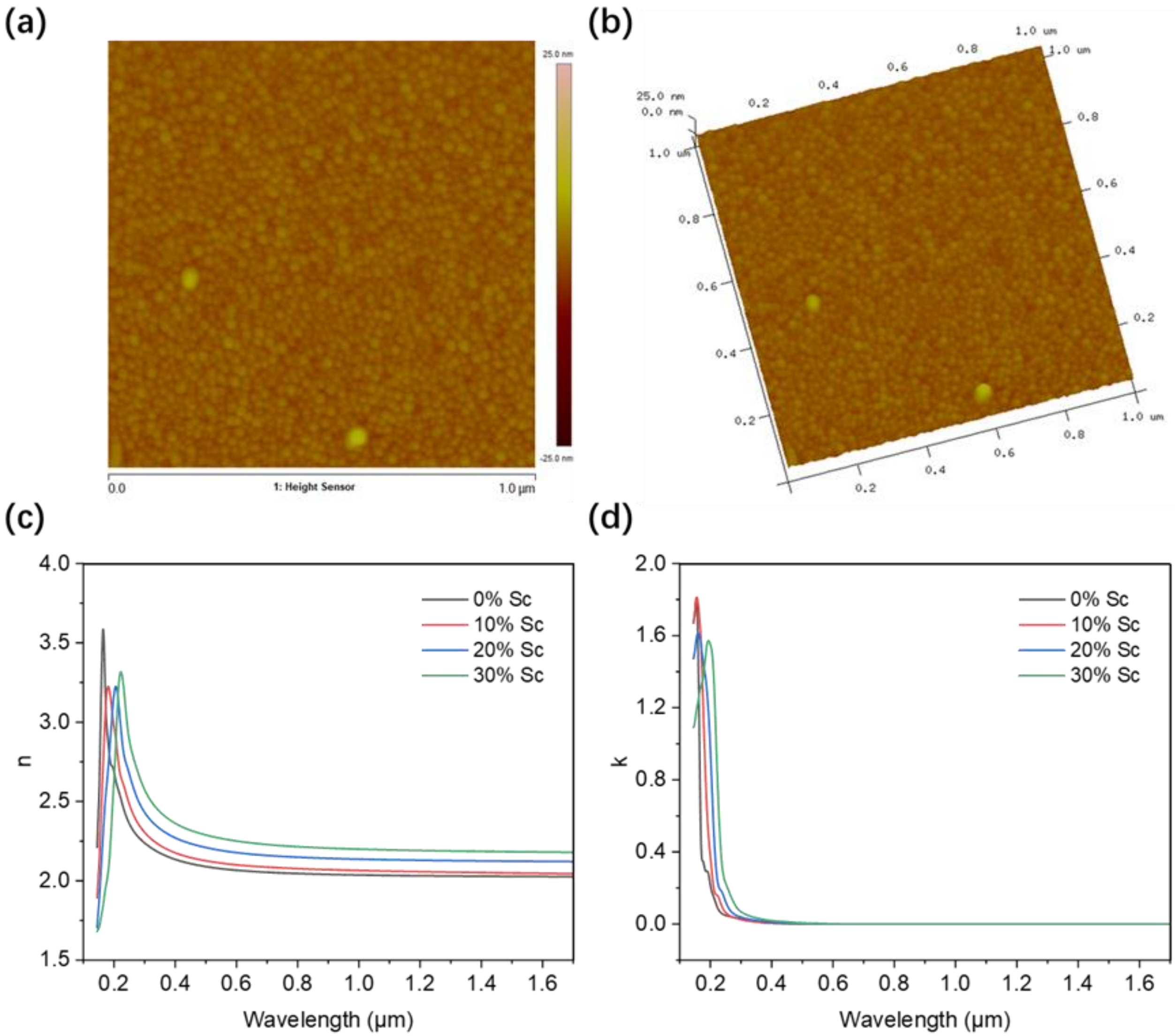


Figure 1. (a, b) 2D and 3D results from AFM measurement of a ScAlN thin film over a 1 × 1 µm² area, showing a polycrystalline surface morphology with an RMS roughness of ~0.8 nm. (c, d) Extracted refractive index n and extinction coefficient k of the ScAlN thin film from spectroscopic ellipsometry measurements.

## PROPAGATION LOSS EXTRACTION USING MICRORING RESONATORS

There are two commonly used approaches to extract the optical propagation loss of integrated waveguides. The first approach is the cutback method, where waveguides with different physical lengths are fabricated and their transmission losses are linearly fitted to obtain the propagation loss per unit length. While this method can effectively mitigate the influence of laser-to-chip coupling losses, it typically requires multiple waveguides with sufficiently different lengths to achieve accurate fitting. Moreover, for waveguides with relatively high propagation loss, the output signal from longer waveguides may become weak or even fall below the detection limit, which significantly degrades the reliability of the extracted loss values.

In this work, we adopt an alternative and widely used approach based on the analysis of microring resonator (MRR) transmission spectra to extract the waveguide propagation loss. Similar to the cutback method, this approach is insensitive to laser-to-chip coupling losses, as the loss extraction relies on resonance characteristics rather than absolute transmission levels. In addition, when the MRR operates near the critical coupling regime, the intrinsic quality factor can be accurately determined, enabling reliable estimation of the waveguide propagation loss. Compared to the cutback method, this approach does not require long waveguides and therefore allows robust spectral measurements even for relatively lossy waveguides.

The propagation loss of the waveguide forming the MRR can be extracted from the intrinsic quality factor $Q_i$ obtained by fitting the resonance linewidth, which can be expressed as:

$$Loss = 10log_{10}\left(e^{\frac{-2\pi n_g}{\lambda Q_i}}\right) \tag{1}$$

where $n_g$ is the group index of the guided mode, which can be extracted from the FSR of MRR ($FSR = \frac{\lambda^2}{n_g L}$). $\lambda$ is the resonance wavelength, and $Q_i$ is the intrinsic quality factor. By extracting $Q_i$ from the measured transmission spectrum and calculating the corresponding group index, the waveguide propagation loss can be quantitatively determined.

Figure 2(a) shows the transmission spectrum of a MRR with a waveguide width of 1 µm and a ring radius of 250 µm. The microring is side-coupled to a straight bus waveguide through a directional coupler with a coupling gap of 0.4 µm and a coupling length of 20 µm. Owing to the presence of the extended directional coupler, the coupling condition varies with wavelength, resulting in pronounced differences in the extinction ratio among individual resonances[36]. As a result, the extinction ratios of the measured resonance peaks span a wide range, from approximately 8 dB to 30 dB.

Each resonance peak is fitted using a Lorentzian lineshape to extract the full width at half maximum (FWHM), from which the loaded quality factor $Q_L$ can be obtained. The intrinsic quality factor $Q_i$ is then calculated from the loaded quality factor and the on-resonance transmission $T_0$ according to[37,38]:

$$Q_i = \frac{2Q_L}{1 \pm \sqrt{T_0}} \tag{2}$$

where the plus and minus signs correspond to the over-coupled and under-coupled regimes, respectively.

Figure 2(b) shows the FWHM of the resonance peak in Fig. 2(a) with an extinction ratio of 29 dB. The measured FWHM is approximately 0.11 nm, corresponding to a loaded quality factor of about 13,500. Under this near–critical coupling condition, the intrinsic quality factor can be reasonably approximated as twice the loaded quality factor.

For this resonance, the center wavelength is 1542.2 nm and the free spectral range (FSR) is measured to be 0.678 nm. By substituting these values into Eq. (1), the waveguide propagation loss is extracted to be approximately 14.6 dB/cm.

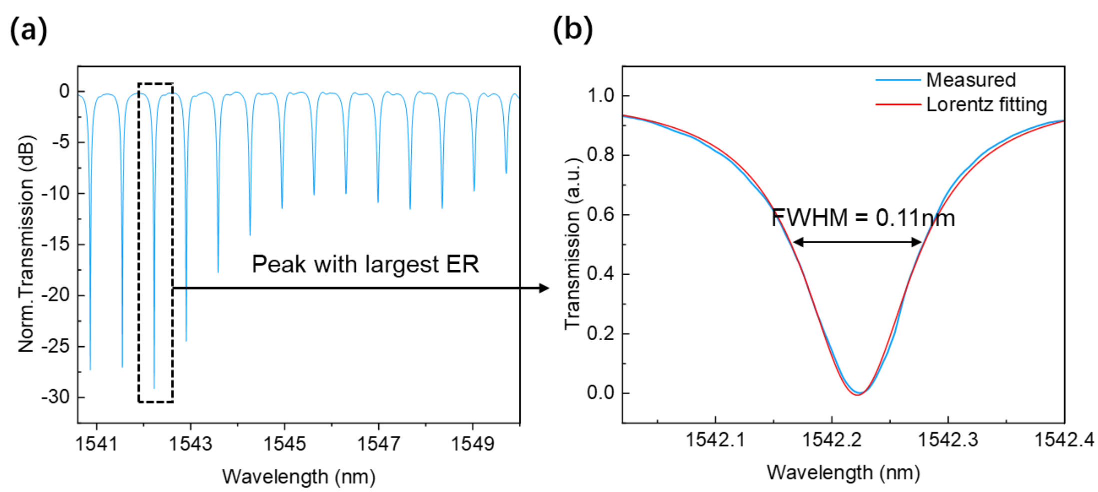


Figure 2. (a) Measured transmission spectrum of a MRR with a 1-µm-wide waveguide and a radius of 250 µm, coupled to a straight bus waveguide through a 20 µm directional coupler. (b) Enlarged view of a representative resonance (extinction ratio: 29 dB) used to extract the loaded and intrinsic quality factors for propagation loss estimation.

## WAFER-SCALE PROPAGATION LOSS CHARACTERIZATION: EFFECTS OF WAVEGUIDE GEOMETRY AND SPATIAL VARIATION

To investigate the impact of waveguide geometry (width and thickness) and wafer-level spatial variation on optical propagation loss, two 8-inch wafers with different ScAlN film thicknesses were fabricated using identical CMOS-compatible processes. Figures 3(a) and 3(b) show the cross-sectional scanning electron microscope (SEM) images of representative waveguides from the two wafers. For the first wafer, the ScAlN waveguide thickness is approximately 450 nm, with a measured sidewall angle of about 80°. In contrast, the second wafer exhibits a thicker ScAlN waveguide of approximately 630 nm, accompanied by a reduced sidewall angle of around 72°, reflecting increased etching challenges associated with thicker films.

Aside from the film thickness and sidewall profile, the two wafers share an identical device layout. Each wafer contains a comprehensive set of microring resonators with systematically varied parameters, including waveguide width, ring radius, coupling gap, and coupling length. These microring resonators are designed to enable reliable extraction of waveguide propagation loss across a wide range of geometries using the resonance-based method described in the previous section.

Figure 3(c) illustrates the schematic of wafer-level sampling locations. Eight representative chip positions distributed across the wafer are selected for loss characterization and comparative analysis, covering both central and peripheral regions of the wafer. This sampling strategy allows us to evaluate not only geometry-dependent loss trends but also spatial variations in film quality and fabrication uniformity.

Table 1 summarizes the extracted propagation losses for the 450-nm-thick wafer at different wafer locations and for multiple waveguide widths. The reported loss values are obtained by analyzing the coupling conditions of individual MRRs and selecting resonance peaks operating close to the critical coupling regime, where the intrinsic quality factor can be extracted with higher accuracy. For each geometry and location, multiple resonances are analyzed to ensure consistency.

The results listed in Table 1 are visualized in Fig. 3(d) for clarity. A clear trend is observed in which the propagation loss increases with increasing waveguide width. In addition, a pronounced wafer-level spatial dependence is evident. Chips located near the wafer edge (C2, D10, G1, and J5) consistently exhibit lower propagation losses, whereas chips closer to the wafer center (E4, F6, and H4) show comparatively higher losses.

| Waveguide thickness (μm) | Waveguide width (μm) | Bending radius (μm) | C2 loss (dB/cm) | D10 loss (dB/cm) | E4 loss (dB/cm) | F6 loss (dB/cm) | G1 loss (dB/cm) | H4 loss (dB/cm) | H8 loss (dB/cm) | J5 loss (dB/cm) |
|---|---|---|---|---|---|---|---|---|---|---|
| 0.45 | 0.8 | 250 | 10.7 | 11.3 | 13.1 | 12.2 | 10.0 | 11.9 | 13.2 | 9.9 |
| | 1 | 250 | 11.0 | 12.3 | 14.0 | 13.5 | 11.6 | 12.7 | 11.6 | 12.6 |
| | 1.5 | 160 | 11.8 | 13.7 | 10.5 | 13.1 | 12.3 | 16.5 | 14.4 | 13.5 |
| | 2 | 160 | 14.6 | 13.1 | 18.6 | 15.6 | 15.8 | 18.2 | 19.2 | 15.7 |
| 0.63 | 0.8 | 250 | 13.0 | 15.6 | 24.3 | 21.2 | 14.9 | 20.0 | 16.6 | 17.0 |
| | 1 | 250 | 14.1 | 14.7 | 25.1 | 20.4 | 14.1 | 20.5 | 18.3 | 14.8 |
| | 1.5 | 160 | 15.9 | 14.8 | 29.4 | 21.8 | 14.3 | 16.5 | 18.8 | 14.0 |
| | 2 | 160 | 18.5 | 15.4 | 26.3 | 23.3 | 14.6 | 22.3 | 19.3 | 13.8 |

Table 1 Extracted optical propagation losses of 450-nm-thick and 630-nm-thick ScAlN waveguides with different widths at selected wafer locations.

Using the same method, the waveguide propagation losses of the 630-nm-thick ScAlN wafer are extracted for different waveguide widths and wafer locations. The statistical results are also summarized in Table 1. Figure 3(d) presents a bar chart visualization of the extracted losses, from which trends similar to those observed for the 450-nm-thick wafer can be identified.

Specifically, the propagation loss generally increases with increasing waveguide width, indicating a geometry-dependent loss behavior that persists across different film thicknesses. In addition, a clear wafer-level spatial dependence is again observed. Chips located near the wafer center (E4, F6, and H4) consistently exhibit higher propagation losses compared to those located closer to the wafer edge.

To directly compare the effect of waveguide thickness, Fig. 3(e) shows the propagation losses of the 450-nm- and 630-nm-thick wafers at identical wafer locations. For each location, the reported loss value is obtained by averaging the extracted losses of four waveguides with different widths. A systematic increase in propagation loss is observed when the waveguide thickness increases from 450 nm to 630 nm, with an average increase of approximately 4 dB/cm across the wafer.

This thickness-dependent increase in propagation loss is attributed primarily to absorption-related mechanisms. As the waveguide cross-sectional area increases with both width and thickness, the optical mode exhibits a larger overlap with the ScAlN material, where residual defects, increased Sc-induced disorder, and material absorption can contribute to higher loss. Consequently, waveguides with larger dimensions experience enhanced absorption loss, leading to the observed increase in propagation loss for thicker ScAlN films.

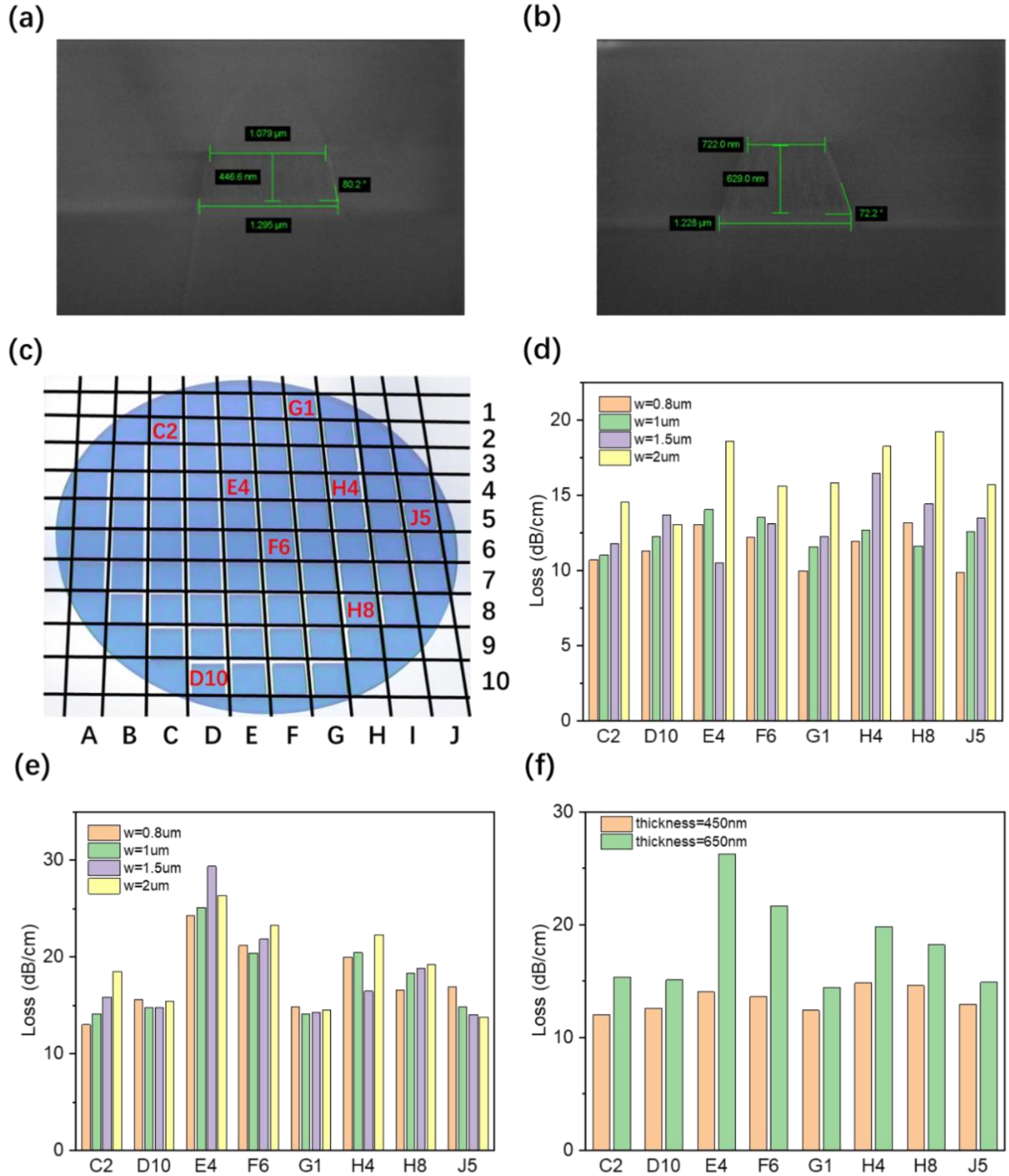


Figure 3. (a, b) Cross-sectional SEM images of ScAlN waveguides with thicknesses of ~450 nm and ~630 nm, respectively. (c) Wafer-level sampling locations for loss characterization. (d) Extracted propagation losses versus waveguide width at different wafer positions. (e) Propagation losses of 630-nm-thick ScAlN waveguides with different widths at various wafer locations. (f) Comparison of averaged propagation losses between 450-nm- and 630-nm-thick ScAlN wafers at identical locations.

## CONCLUSION

In summary, we have presented a wafer-scale characterization of optical propagation loss in 10% Sc-doped aluminum nitride (ScAlN) waveguides fabricated on CMOS-compatible 8-inch wafers. Propagation losses are extracted using microring resonators operating near the critical coupling regime, enabling reliable loss evaluation without being affected by laser-to-chip coupling variations. In parallel, material properties of the ScAlN films are characterized through AFM and spectroscopic ellipsometry, providing insight into surface quality and intrinsic optical absorption.

The results reveal clear dependencies of propagation loss on waveguide geometry and wafer location. For both 450-nm- and 630-nm-thick ScAlN films, the propagation loss generally increases with increasing waveguide width, and higher losses are consistently observed for devices located near the wafer center. In addition, increasing the waveguide thickness from 450 nm to 630 nm leads to an average loss increase of approximately 4 dB/cm. These trends indicate enhanced absorption due to increased optical mode overlap with the material.

Overall, the combined device-level and material characterization indicates that absorption-related loss currently dominates the propagation loss in ScAlN waveguides at this doping concentration. Further loss reduction is therefore expected through continued optimization of film deposition quality, including improved crystallinity, reduced defect density, and enhanced compositional uniformity, providing a clear pathway toward low-loss, wafer-scale ScAlN photonic platforms for high-efficiency electro-optic applications.

## ACKNOWLEDGEMENTS

This work is supported by Agency for Science, Technology and Research under grant no. M23M5a0069 for device fabrication, M23M6c0109 for results analysis, and National Research Foundation (NRF) under grant no. NRF-F-CRP-2024-0006 for device characterization. The authors appreciate Nina Hong for assistance on ellipsometry measurement and discussion, and Yunjie Chen for assistance on AFM measurement. We used ChatGPT (OpenAI) to improve the readability and language of this manuscript; all substantive content and conclusions were developed by the authors.

## REFERENCES

[1] Zhou, H., Li, D. and Lee, C., "Technology Landscape Review of In-Sensor Photonic Intelligence: From Optical Sensors to Smart Devices," AI Sensors **1**(1), 5 (2025).

[2] Liu, X., Bruch, A. W. and Tang, Hong. X., "Aluminum nitride photonic integrated circuits: from piezo-optomechanics to nonlinear optics," Advances in Optics and Photonics **15**(1), 236 (2023).

[3] Li, J., Xu, K. and Du, J., "Ultrabroadband and Flattened Dispersion in Aluminum Nitride Slot Waveguides," IEEE Photonics Journal **9**(4) (2017).

[4] Li, N., Ho, C. P., Zhu, S., Fu, Y. H., Zhu, Y. and Lee, L. Y. T., "Aluminium nitride integrated photonics: a review," Nanophotonics **10**(9), 2347–2387 (2021).

[5] Lu, T.-J., Fanto, M., Choi, H., Thomas, P., Steidle, J., Mouradian, S., Kong, W., Zhu, D., Moon, H., Berggren, K., Kim, J., Soltani, M., Preble, S. and Englund, D., "Aluminum nitride integrated photonics platform for the ultraviolet to visible spectrum," Optics Express **26**(9), 11147 (2018).

[6] Xiong, C., Pernice, W. H. P. and Tang, H. X., "Low-Loss, Silicon Integrated, Aluminum Nitride Photonic Circuits and Their Use for Electro-Optic Signal Processing," Nano Letters **12**(7), 3562–3568 (2012).

[7] Guo, X., Zou, C.-L. and Tang, H. X., "Second-harmonic generation in aluminum nitride microrings with 2500%/W conversion efficiency," Optica **3**(10), 1126 (2016).

[8] Liu, X., Sun, C., Xiong, B., Wang, L., Wang, J., Han, Y., Hao, Z., Li, H., Luo, Y., Yan, J., Wei, T., Zhang, Y. and Wang, J., "Generation of multiple near-visible comb lines in an AlN microring via $\chi$ (2) and $\chi$ (3) optical nonlinearities," Applied Physics Letters **113**(17) (2018).

[9] Li, N., Zhuge, Y., Chung, W. W., Xu, S., Cao, Y., Quek, Z. J., Tobing, L. Y. M., Ho, C. P., Tan, D. T. H., Lee, C. and Luo, X., "Broadband Frequency Comb Generation on CMOS-Compatible 8-inch Aluminum Nitride Photonics Platform," CLEO 2025, SS185_5, Optica Publishing Group, Washington, D.C. (2025).

[10] Zhuge, Y., Ren, Z., Xiao, Z., Zhang, Z., Liu, X., Liu, W., Xu, S., Ho, C. P., Li, N. and Lee, C., "Photonic Bayesian Neural Networks: Leveraging Programmable Noise for Robust and Uncertainty-Aware Computing," Advanced Science **12**(23) (2025).

[11] Ren, Z., Zhang, Z., Zhuge, Y., Xiao, Z., Xu, S., Zhou, J. and Lee, C., "Near-Sensor Edge Computing System Enabled by a CMOS Compatible Photonic Integrated Circuit Platform Using Bilayer AlN/Si Waveguides," Nano-Micro Letters **17**(1), 261 (2025).

[12] Dong, B., Zhang, Z., Shi, Q., Wei, J., Ma, Y., Xiao, Z. and Lee, C., "Biometrics-protected optical communication enabled by deep learning–enhanced triboelectric/photonic synergistic interface," Science Advances **8**(3), 1–14 (2022).
[13] Li, N., Lim, L. W., Xue, J., Ho, C. P., Zhu, S., Fu, Y. H. and Lee, L. Y. T., "Aluminum Nitride Nanophotonic Phased Array on an 8-inch Silicon Wafer," CLEO 2023, AM3M.5, Optica Publishing Group, Washington, D.C. (2023).
[14] Jung, H., Stoll, R., Guo, X., Fischer, D. and Tang, H. X., "Green, red, and IR frequency comb line generation from single IR pump in AlN microring resonator," Optica **1**(6), 396 (2014).
[15] Li, N., Ho, C. P., Cao, Y., Zhu, S., Chen, G. F. R., Fu, Y. H., Zhu, Y., Tan, D. T. H. and Lee, L. Y. T., "Aluminum Nitride Photonics Platforms on Silicon Substrate," CLEO 2021, STh2H.3, Optica Publishing Group, Washington, D.C. (2021).
[16] Wang, C., Zhang, M., Chen, X., Bertrand, M., Shams-Ansari, A., Chandrasekhar, S., Winzer, P. and Lončar, M., "Integrated lithium niobate electro-optic modulators operating at CMOS-compatible voltages," Nature **562**(7725), 101–104 (2018).
[17] Hu, Y., Zhu, D., Lu, S., Zhu, X., Song, Y., Renaud, D., Assumpcao, D., Cheng, R., Xin, C. J., Yeh, M., Warner, H., Guo, X., Shams-Ansari, A., Barton, D., Sinclair, N. and Loncar, M., "Integrated electro-optics on thin-film lithium niobate," Nature Reviews Physics **7**(5), 237–254 (2025).
[18] Lončar, M., "Integrated Lithium Niobate Photonics and Applications," 2023 28th Microoptics Conference (MOC) **9**(6), 1–2, IEEE (2023).
[19] Chen, G., Li, N., Ng, J. Da, Lin, H.-L., Zhou, Y., Fu, Y. H., Lee, L. Y. T., Yu, Y., Liu, A.-Q. and Danner, A. J., "Advances in lithium niobate photonics: development status and perspectives," Advanced Photonics **4**(03), 1–43 (2022).
[20] Zhu, D., Shao, L., Yu, M., Cheng, R., Desiatov, B., Xin, C. J., Hu, Y., Holzgrafe, J., Ghosh, S., Shams-Ansari, A., Puma, E., Sinclair, N., Reimer, C., Zhang, M. and Lončar, M., "Integrated photonics on thin-film lithium niobate," Advances in Optics and Photonics **13**(2), 242 (2021).
[21] Zhu, S., Zhong, Q., Hu, T., Li, Y., Xu, Z., Dong, Y. and Singh, N., "Aluminum Nitride Ultralow Loss Waveguides and Push-Pull Electro-Optic Modulators for Near Infrared and Visible Integrated Photonics," Optical Fiber Communication Conference (OFC) 2019, W2A.11, Optical Society of America, San Diego, California (2019).
[22] Yang, G., Wang, H., Mu, S., Xie, H., Wang, T., He, C., Shen, M., Liu, M., Van de Walle, C. G. and Tang, H. X., "Unveiling the Pockels coefficient of ferroelectric nitride ScAlN," Nature Communications **15**(1), 9538 (2024).
[23] Bian, K., Li, Z., Liu, Y., Xu, S., Zhao, X., Qiu, Y., Dong, Y., Zhong, Q., Wu, T., Zheng, S. and Hu, T., "Demonstration of acousto-optical modulation based on a thin-film AlScN photonic platform," Photonics Research **12**(6), 1138 (2024).
[24] Wang, D., Wang, P., Mondal, S., Liu, J., Hu, M., He, M., Nam, S., Peng, W., Yang, S., Wang, D., Xiao, Y., Wu, Y., Mortazawi, A. and Mi, Z., "Controlled ferroelectric switching in ultrawide bandgap AlN/ScAlN multilayers," Applied Physics Letters **123**(10) (2023).
[25] Wang, S., Li, B., Zhou, L., Leong, V., Li, N., Luo, X. and Zhu, D., "Monolithic Integration of ScAlN Modulators on Silicon-On-Insulator Platform," Laser & Photonics Reviews, e02672 (2025).
[26] Xu, T., Liu, Y., Pu, Y., Yang, Y., Zhong, Q., Zhao, X., Qiu, Y., Dong, Y., Wu, T., Zheng, S. and Hu, T., "Silicon-integrated scandium-doped aluminum nitride electro-optic modulator," Photonics Research **13**(2), 477 (2025).
[27] Zhu, S., Zhong, Q., Li, N., Hu, T., Dong, Y., Xu, Z., Zhou, Y., Fu, Y. H. and Singh, N., "Integrated ScAlN Photonic Circuits on Silicon Substrate," CLEO 2020, STu3P.5, Optical Society of America, Washington, DC (2020).
[28] Bian, K., Li, Z., Zhao, X., Qiu, Y., Zheng, S., Dong, Y., Zhong, O. and Hu, T., "Integrated Scandium-Doped Aluminum Nitride Microring Resonators on 8-Inch Silicon Wafers," 2023 Asia Communications and Photonics Conference/2023 International Photonics and Optoelectronics Meetings (ACP/POEM), 1–5, IEEE (2023).
[29] Xiong, Z., Zhang, X., Li, Z., Liu, X., Qiu, Y., Zhao, X., Zheng, S., Zhong, Q., Dong, Y. and Hu, T., "Aluminum scandium nitride on 8-inch Si wafers: material characterization and photonic device demonstration," Optics Express **32**(10), 17525 (2024).
[30] Li, Z., Bian, K., Chen, X., Zhao, X., Qiu, Y., Dong, Y., Zhong, Q., Zheng, S. and Hu, T., "Demonstration of Integrated AlScN Photonic Devices on 8-Inch Silicon Substrate," Journal of Lightwave Technology **42**(14), 4933–4938 (2024).
[31] Spettel, J., Andrianov, N., Dubois, F., Azeem, M., Furci, H., Cassese, T., Quack, N., Villanueva, G., Moridi, M. and Dao, T. D., "Ultraviolet to mid-infrared optical properties of sputtered Al(Sc)N-on-SiO 2 thin films and experimental demonstration of AlN integrated photonic devices in the telecom C-band," Optics Express **32**(24), 42529 (2024).

[32] Li, N., Zhuge, Y., Chung, W. W., Gong, X., Xu, S., Cao, Y., Li, M., Tsang, Y. F., Toh, Y. T., Lee, S. H. J., Lin, H., Tobing, L. Y., Ho, C. P., Chae, S. H., Luo, X. and Lee, C., "Optical properties of scandium-doped aluminum nitride thin film for integrated photonics," Integrated Optics: Devices, Materials, and Technologies XXIX, S. M. García-Blanco and P. Cheben, Eds., 54, SPIE (2025).

[33] Li, N., Chung, W. W., Goh, J. S., Tsang, Y. F., Tobing, L. Y. M., Ho, C. P., Varghese, B., Lim, L. W., Li, M., Lin, H., Zhang, Q., Ng, D. K. T., Lee, L. Y. T. and Luo, X., "Scandium-doped aluminum nitride photonic integration platform," Integrated Optics: Devices, Materials, and Technologies XXVIII, S. M. García-Blanco and P. Cheben, Eds., 42, SPIE (2024).

[34] Wang, S., Dhyani, V., Mohanraj, S. S., Shi, X., Varghese, B., Chung, W. W., Huang, D., Lim, Z. S., Zeng, Q., Liu, H., Luo, X., Leong, V., Li, N. and Zhu, D., "CMOS-compatible photonic integrated circuits on thin-film ScAlN," APL Photonics **9**(6) (2024).

[35] Friedman, B., Barth, S., Schreiber, T., Bartzsch, H., Bain, J. and Piazza, G., "Measured optical losses of Sc doped AlN waveguides," Optics Express **32**(4), 5252 (2024).

[36] Delage, A., Xu, D.-X., McKinnon, R. W., Post, E., Waldron, P., Lapointe, J., Storey, C., Densmore, A., Janz, S., Lamontagne, B., Cheben, P. and Schmid, J. H., "Wavelength-Dependent Model of a Ring Resonator Sensor Excited by a Directional Coupler," Journal of Lightwave Technology **27**(9), 1172–1180 (2009).

[37] Leo, J., Hayati, M., Agri, F. E., Haddad, Z., Choong, G., Petremand, Y., Prieto, I., Dubochet, O., Despont, M., Sattari, H. and Ghadimi, A., "Wafer-scale fabrication of low-loss waveguides in lithium niobate on insulator (LNOI) integrated photonics platform," 2022 European Conference on Optical Communication, ECOC 2022 (2022).

[38] Rabiei, P., Steier, W. H., Cheng Zhang and Dalton, L. R., "Polymer micro-ring filters and modulators," Journal of Lightwave Technology **20**(11), 1968–1975 (2002).